RESULTS AND DISCUSSION

1. Particular Interaction between Pyrimethamine Derivatives and Quadruple Mutant Type Dihydrofolate Reductase of *Plasmodium Falciparum*: CoMFA and Quantum Chemical Calculations Studies

1.1 Statistical Analysis

The relationship between structural properties of twenty-three Pyr derivatives and their biological activities of quadruple mutant type *Pf*DHFR is presented by using the CoMFA model. There are three models that varied the type of probe atoms C_{sp3} (+1), O_{sp3} (-1) and H (+1) and the statistical results are shown in Table 5. All models can be used to well predict the pK_i values for training compounds, with a residual not greater than 0.4; these results are summarized in Table 6. Evaluation of the model prediction is assessed by test set compounds which all showed acceptable pK_i prediction values, except compound **23**; this test set compound has a different structure of **R** substitution ($(CH_2)_2O(CH_2)_3OPh$) from the others, so it shows high residual pK_i between actual and predicted values.

Table 5 PLS statistical results of CoMFA models for quadruple mutant *Pf*DHFR

Parameters	**Probe Atoms**			
	Model I	**Model II**	**Model III**	**Model IV**
	C_{sp3} (+1)	**O_{sp3} (-1)**	**H (+1)**	**C_{sp3} (+1)O_{sp3} (-1)H (+1)**
no of molecules in training set	18	18	18	18
r^2_{cv}	0.724	0.669	0.690	0.702
S_{press}	0.560	0.641	0.620	0.608
no of components	5	6	6	6
r^2_{nv}	0.963	0.980	0.983	0.980
s	0.206	0.157	0.144	0.156
F value	62.152	90.708	108.191	92.183
Steric field contributions	0.613	0.567	0.519	0.547
Electrostatic field contributions	0.387	0.433	0.481	0.453
$r^2_{test\text{-}set}$	0.495	0.566	0.695	0.698

Table 6 Actual (Act) and predicted (Pred) pK_i values and the residuals (Δ) of the training set and test set molecules for the mutant *Pf*DHFR models

Comp	Act	Model I		Model II		Model III		Model IV	
	p*Ki*	Pred p*Ki*	Δ	Pred p*Ki*	Δ	Pred p*Ki*	Δ	Pred p*Ki*	Δ
1	6.41	6.28	0.13	6.38	0.03	6.32	0.09	6.36	0.05
3	6.55	6.53	0.01	6.61	-0.07	6.61	-0.06	6.67	-0.13
4	7.27	7.58	-0.31	7.38	-0.10	7.31	-0.04	7.38	-0.10
6	8.48	8.12	0.36	8.16	0.32	8.24	0.23	8.16	0.32
7	6.44	6.54	-0.09	6.36	0.08	6.46	-0.01	6.35	0.09
8	7.62	7.50	0.11	7.77	-0.15	7.69	-0.07	7.77	-0.15
11	8.33	8.12	0.21	8.24	0.08	8.19	0.13	8.23	0.10
12	8.70	8.82	-0.12	8.79	-0.09	8.73	-0.04	8.79	-0.09
13	6.26	6.38	-0.12	6.44	-0.18	6.53	-0.27	6.45	-0.19
14	7.24	7.06	0.18	7.06	0.18	7.14	0.11	7.08	0.16
15	6.62	6.75	-0.13	6.60	0.02	6.51	0.11	6.57	0.06
16	7.50	7.38	0.12	7.40	0.10	7.41	0.09	7.44	0.06
17	7.85	7.91	-0.06	7.87	-0.02	7.85	-0.00	7.86	-0.01
18	8.44	8.45	-0.01	8.47	-0.02	8.52	-0.07	8.48	-0.04
19	8.85	8.78	0.07	8.86	-0.01	8.94	-0.09	8.89	-0.03
20	8.44	8.44	0.00	8.45	-0.01	8.42	0.02	8.44	0.01
21	7.85	8.15	-0.30	8.01	-0.16	7.95	-0.10	7.96	-0.11
22	8.70	8.77	-0.07	8.70	-0.00	8.74	-0.04	8.71	-0.01
2[a]	6.57	6.74	-0.17	6.76	-0.19	6.75	-0.18	6.75	-0.18
5[a]	7.49	6.89	0.60	7.28	0.21	7.31	0.18	7.26	0.23
9[a]	8.57	8.00	0.57	7.92	0.65	8.29	0.28	7.96	0.61
10[a]	6.77	7.63	-0.86	7.41	-0.64	7.38	-0.61	7.44	-0.67
23[a]	8.77	9.31	-0.54	9.81	-1.04	9.87	-1.10	9.65	-0.88

[a] Test set compounds

By considering the statistical results in Table 4, model I-III with r^2_{cv} values higher than 0.6 (0.724, 0.669 and 0.690, respectively) can be accepted and the conventional r^2 or no-validated r^2 (r^2_{nv}) values are found to be 0.963, 0.980 and 0.983, respectively. These mean that the three tested probes (C_{sp3}, O_{sp3} and H) give qualitatively very similar models. The results suggest that all three types of probes form equally important in the enzyme-ligand interactions. Next, the combination of

three probe atoms was used, resulting in model IV with r^2_{cv} = 0.702 and r^2_{nv} = 0.980. Moreover, the prediction for test set obtained from model IV shows the highest predictive ability ($r^2_{test\ set}$ = 0.698). Therefore, the combining three probe atoms in model IV is superior and more general model. Especially, the statistical error (s) of the represented model is 0.156 which is reasonably acceptable for biological activity predictions of the training set and the test set. The graphical plot between actual and predicted pK_i of the training set and the test set is shown in Figure 21. The CoMFA field contributions of the steric and electrostatic interactions contributed approximately 50%. The results indicate that both steric and electrostatic contributions are equivalent that affected the biological activity of mutant *Pf*DHFR.

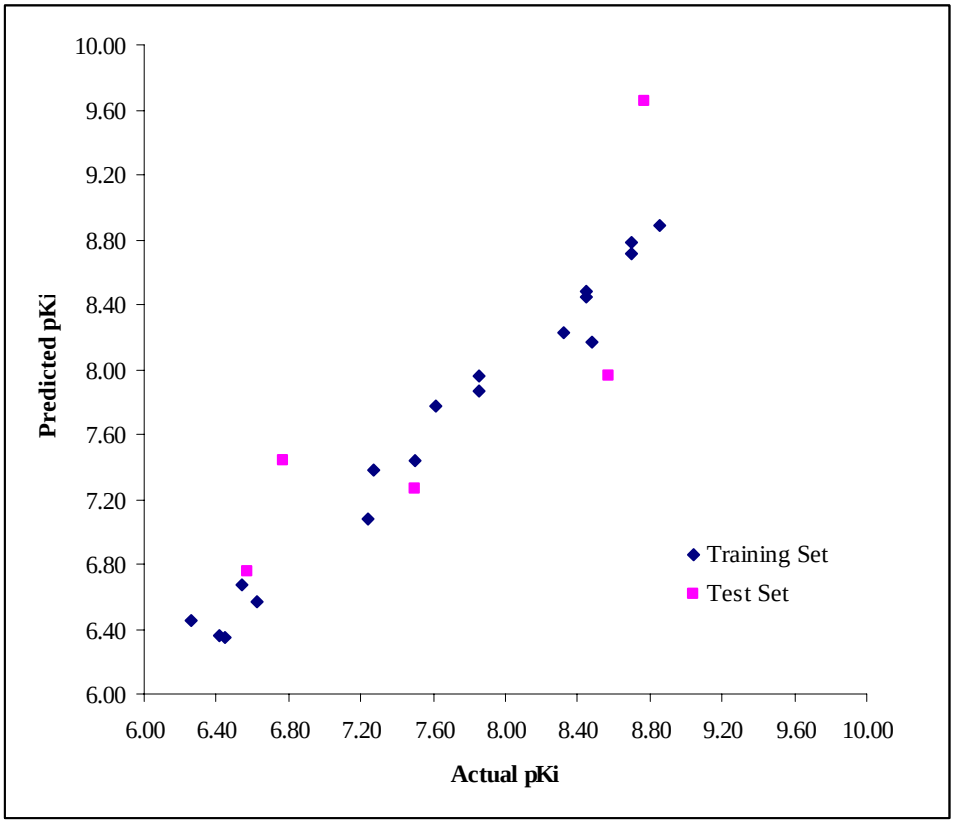

Figure 21 Plot of the predicted and actual pK_i values of the training set and the test set molecules with CoMFA model IV

1.2 CoMFA Contour Analyses

The CoMFA analysis with hundreds or thousands terms, is usually represented as the scalar product of the associated coefficient and the standard deviation of all values in the corresponding column of the data table (STDEV*COEFF) contour plots. Moreover, the contour maps can be showed by merging with the binding pocket of a drug target. In this study, the CoMFA contour maps are merged with 4 Å of binding pocket of crystal structure of quadruple mutant type *Pf*DHFR which is available in the Protein Data Bank with PDB code 1J3K (Yuvaniyama, *et al.*, 2003). The template compound **12** is displayed as the inhibitor in the CoMFA contour maps.

Figure 22 shows the steric contour maps of CoMFA model IV. The steric contour map indicates areas in which molecular steric bulk might have a favourable (green) or unfavourable (yellow) effect on the activity of an analogue. A sterically favoured green region is found near **X** substituent of the aromatic ring. This is further supported by comparing **X** substituent with Cl and H when these compounds have the same **Y** and **R** substituents. In addition, the distribution of steric contours appears around the phenyl sidechain of **R** substituent; this evidence would explain why compound **12**, used as the template, is a better quadruple mutant *Pf*DHFR inhibitor than the Pyr drug (compound **1**). Furthermore, this region is closed to Phe116 of the binding pocket. An unfavourable steric contour region is found at **Y** substituent on the aromatic ring which can explain the fact that compounds **1**, **7** and **10** show lower pK_i when compared with unsubstituted structures of compounds **5**, **8** and **11**, respectively. Therefore, a hydrogen atom is suitable substituent of **Y** position because the unfavourable steric area of **Y** is closed to an important mutation position, Asn108, of quadruple mutant *Pf*DHFR. The obtained unfavourable steric contour coincides with the previous publications that reported a steric clash between the Cl substituent of Pyr and the side chain of Asn108.

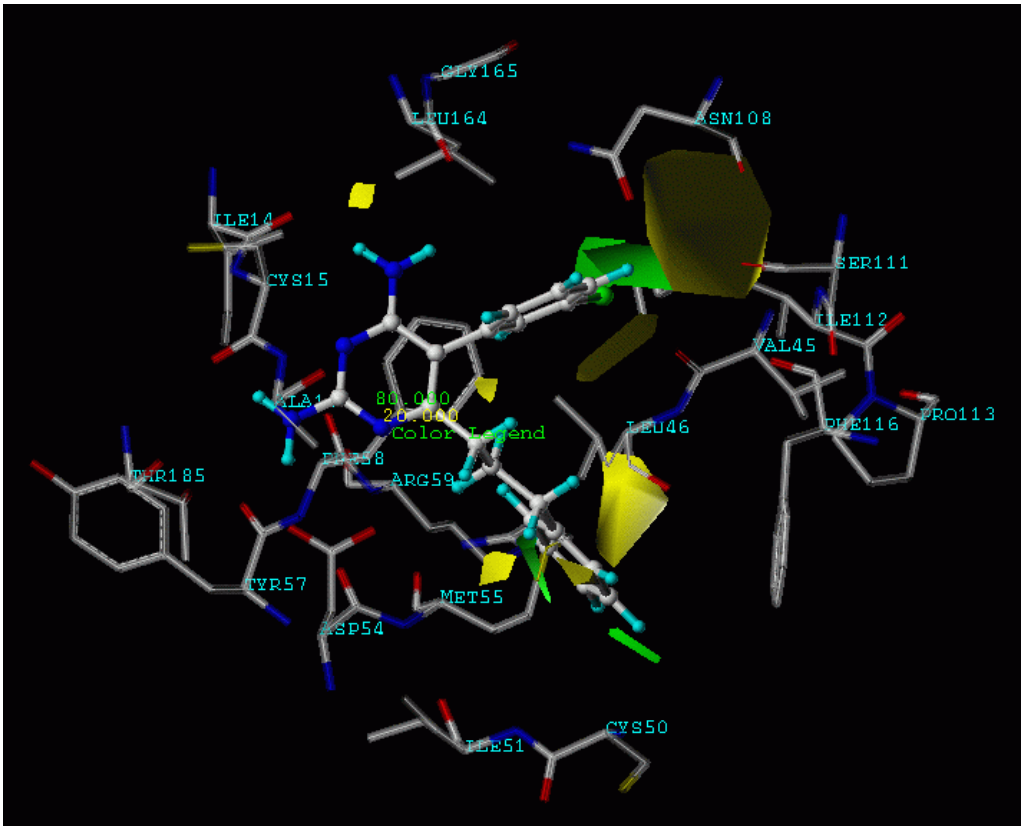

Figure 22 CoMFA (stdev.*coeff.) sterically favored areas are represented by green regions. Sterically unfavored areas are represented by yellow regions (level of steric contour contribution = 80%) and compound **12** is represented by ball and stick.

Figure 23 depicts electrostatic contour maps of CoMFA. The electrostatic contour map reveals that blue contours refer to positive charge favouring areas and red contours indicate negative charge favouring areas. The red area is found in the middle of the phenyl ring of **R** substitution which means high electron density in this area. Furthermore, a large blue contour also surrounds the phenyl ring of **R** substitution. It can be suggested that high positive charges or low electron density in this area is preferable. Therefore, donating substituents of the phenyl ring will increase the activity of the inhibitors, for example, Cl, F, OCH_3, etc.

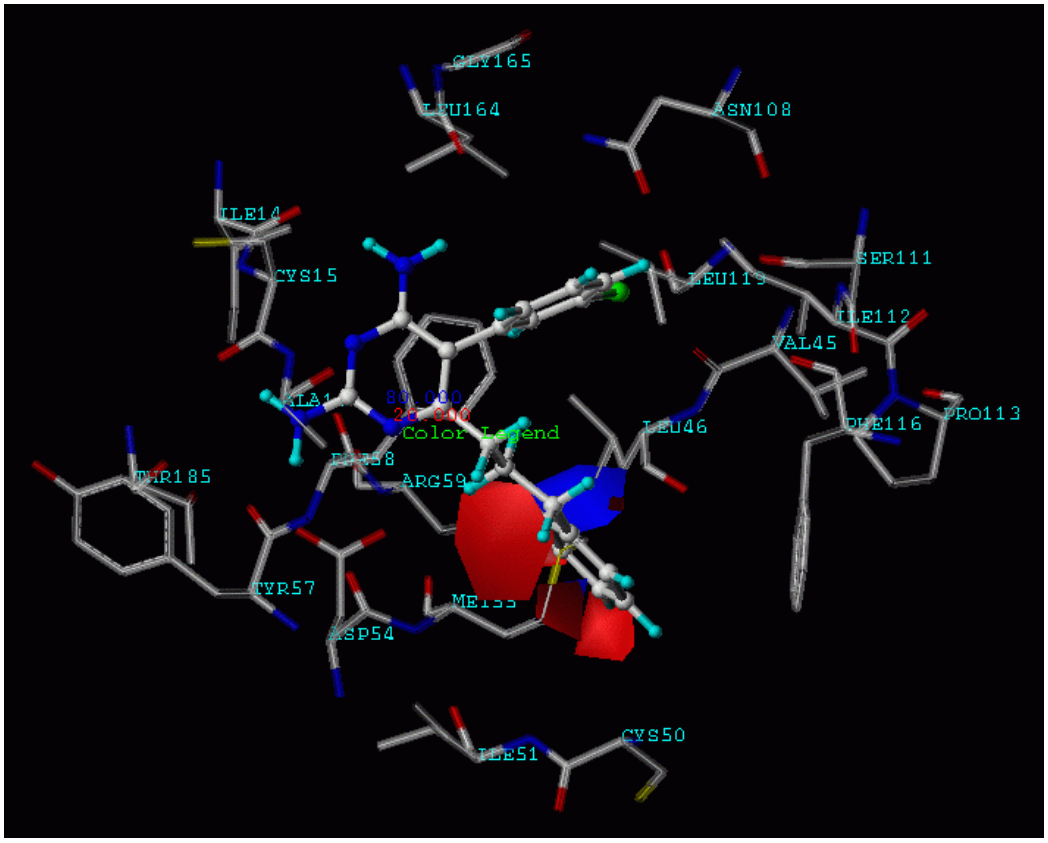

Figure 23 CoMFA (stdev.*coeff.) negative charge favored area is represented by the red region. Positive charge favored area is represented by the blue region (level of electrostatic contour contribution = 80%) and compound **12** is represented by ball and stick.

1.3 Particular interaction energy

In order to find the particular interaction energy between compound **1** or **6** and the amino acids surrounding the pocket of quadruple mutant type *Pf*DHFR, the MP2 method with basis set 6-31G(d,p) level of calculations was performed. In addition, the BSSE-CP was also calculated to correct the interaction energy. The obtained interaction energies are given in Table 7. Asp54 has the strongest interaction energy to compounds **1** and **6** of -10.139 and -10.250 kcal/mol, respectively. This

amino acid formed H-bond interaction with the inhibitors. In addition, the H-bond interactions are also found with Ile14 and Leu164 for both compounds **1** and **6**. All H-bond distances are displayed in Figure 24.

Table 7 Particular interaction energy (kcal/mol) of **1** and **6** with individual residues, calculated by MP2/6-31G(d,p) and MP2/6-31G(d,p) with BSSE-CP.

Amino Acids	Particular Interaction Energy (kcal/mol)			
	Compound 1		Compound 6	
	MP2/6-31G(d,p)	MP2/6-31G(d,p) with BSSE-CP	MP2/6-31G(d,p)	MP2/6-31G(d,p) with BSSE-CP
Ile14	-8.034	-4.172	-8.735	-4.298
Cys15	-4.654	-1.203	-4.737	-1.272
Ala16	-2.122	-0.667	-2.194	-0.506
Val45	-0.183	-0.183	0.002	0.002
Leu46	-0.096	1.223	-1.517	-0.878
Trp48	-0.535	-0.526	-0.554	-0.548
Cys50	-0.063	-0.063	-0.025	-0.025
Ile51	0.044	0.044	0.056	0.056
Asp54	-17.159	-10.139	-17.251	-10.250
Met55	0.191	1.856	0.303	1.933
Tyr57	-0.489	-0.317	-0.343	-0.226
Phe58	-9.634	-3.884	-9.511	-3.326
Arg59	-1.476	-1.475	-1.744	-1.743
Asn108	1.173	3.839	-3.355	-0.895
Ser111	0.085	1.862	-0.921	-0.758
Ile112	0.239	1.790	1.517	2.237
Pro113	-0.118	-0.114	0.038	0.038
Phe116	-0.085	-0.085	0.052	0.052
Leu119	-0.233	-0.219	-0.247	0.531
Leu164	-5.888	-3.470	-4.072	-2.165
Gly165	-0.062	-0.022	0.026	0.071
Thr185	-0.538	0.171	-0.458	0.202

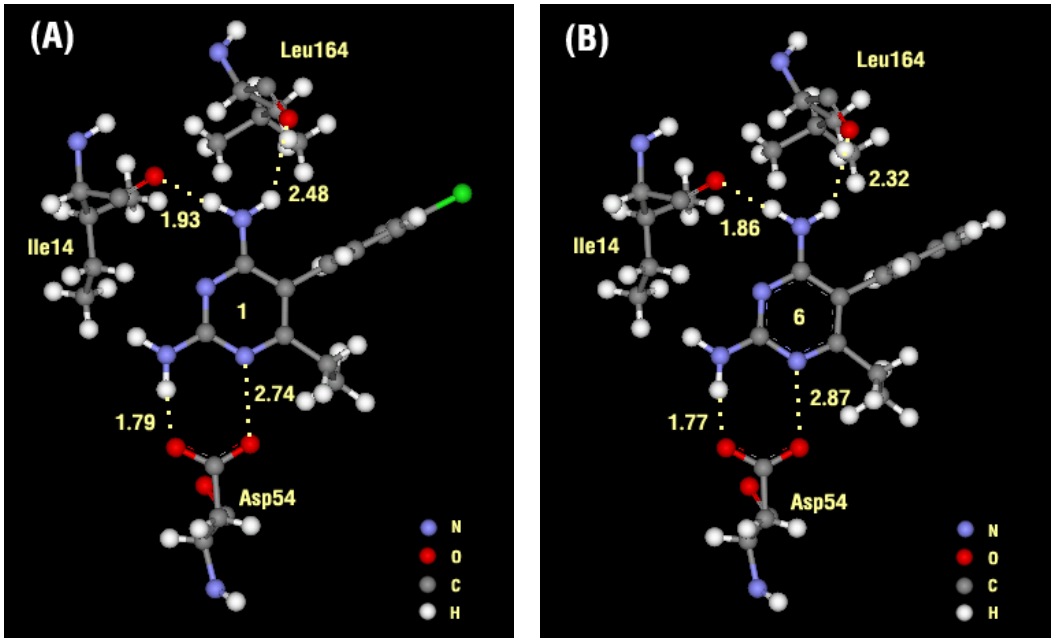

Figure 24 H-bond distances between inhibitor and residues in the binding pocket; (A) compound **1** and (B) compound **6** (in Å).

Three mutant amino acids, Ile51, Arg59 and Leu164, show no significantly different interaction energies between compound **1** and **6** (Table 6). While Asn108 shows more repulsive interaction to compound **1** by approximately 5 kcal/mol because compound **1** has the Cl substituent at **Y** position which can occur due to the steric clash with the side chain of Asn108, as shown clearly by electrostatic potential surfaces in Figure 25. In previous reviews, there were many reports that proposed the cause of Pyr resistance in quadruple mutant type *Pf*DHFR came from the steric clash with Asn108 mutation. Our particular interaction energy studies can verify this evidence with the obtained repulsive energy.

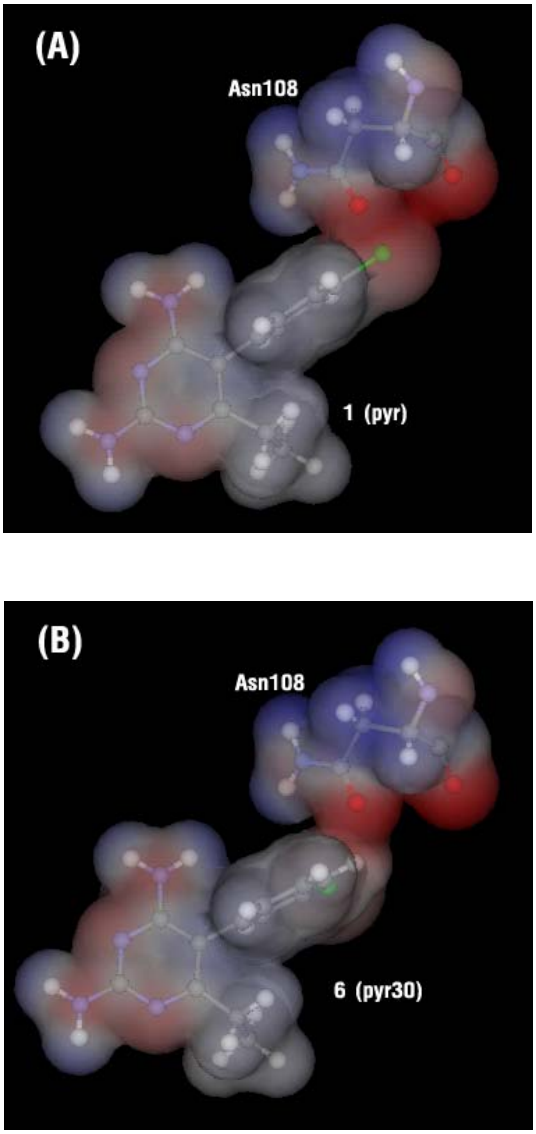

Figure 25 The electrostatic potential is shown on the solvent accessible surface as red for negative and blue for positive values for Asn108 interacted with (A) compound **1** (B) and compound **6**.

2. Interactions between Cycloguanil Derivatives and Wild-Type and Resistance-Associated Mutant *P. Falciparum* Dihydrofolate Reductases

2.1 CoMFA statistical results

Statistically significant CoMFA models were derived from the Cyc derivatives active against the wild type and the quadruple mutant type *Pf*DHFRs. Each CoMFA target enzyme was varied by changing the type of probe atoms at the grid spacings as represented of the receptor. The obtained statistical CoMFA models are reported in Table 8. The predicted pK_i values of wild type and quadruple muatant type models are listed in Table 9 and Table 10, respectively.

Table 8 PLS statistical results of CoMFA models of Cyc derivatives active against wild type and quadruple mutant type *Pf*DHFRs

Parameters	**Wild-type *Pf*DHFR**			**Quadruple mutant *Pf*DHFR**			
	Model I	**Model II**	**Model III**	**Model IV**	**Model V**	**Model VI**	**Model VII**
	C_{sp3} (+1)	**O_{sp3} (-1)**	**H (+1)**	**C_{sp3} (+1)**	**O_{sp3} (-1)**	**H (+1)**	**combined**
r^2_{cv}	0.650	0.645	0.727	0.786	0.729	0.676	0.786
S_{press}	0.365	0.368	0.322	0.682	0.713	0.837	0.650
noc	6	6	6	6	4	6	5
r^2_{nv}	0.977	0.979	0.985	0.983	0.962	0.986	0.979
s	0.094	0.090	0.075	0.192	0.267	0.171	0.202
F value	91.085	99.690	144.780	125.390	95.141	157.924	132.386
%Steric	0.604	0.596	0.565	0.674	0.682	0.644	0.678
%Electrostatic	0.396	0.404	0.435	0.326	0.318	0.356	0.322

Table 9 Actual (Act) and predicted (Pred) pK_i values and the residuals (Δ) of the training set and test set molecules for the wild type models.

Comp	Act p*Ki*	Model I		Model II		Model III	
		Pred p*Ki*	Δ	Pred p*Ki*	Δ	Pred p*Ki*	Δ
1	8.82	8.78	0.04	8.77	0.05	8.78	0.04
2	8.52	8.60	-0.08	8.57	-0.05	8.55	-0.03
4	7.59	7.39	0.20	7.39	0.20	7.43	0.16
5	7.43	7.61	-0.17	7.61	-0.18	7.67	-0.23
6	8.33	8.21	0.12	8.24	0.09	8.27	0.06
7	9.22	9.13	0.09	9.10	0.12	9.11	0.11
8	8.62	8.68	-0.06	8.75	-0.13	8.82	-0.20
9	8.38	8.36	0.02	8.38	0.00	8.35	0.03
11	8.34	8.34	0.00	8.33	0.01	8.24	0.10
12	7.93	8.06	-0.13	8.07	-0.14	8.03	-0.10
13	9.39	9.41	-0.02	9.42	-0.03	9.40	-0.01
14	9.15	9.12	0.03	9.14	0.01	9.14	0.01
16	8.95	8.99	-0.03	8.98	-0.03	8.99	-0.04
17	9.15	9.13	0.02	9.15	-0.00	9.17	-0.02
18	8.63	8.63	0.00	8.61	0.03	8.61	0.02
20	8.88	8.87	0.01	8.87	0.01	8.90	-0.02
21	8.56	8.61	-0.05	8.56	0.00	8.48	0.09
23	8.74	8.71	0.03	8.71	0.03	8.73	0.01
24	8.39	8.42	-0.03	8.41	-0.02	8.40	0.00
25	8.56	8.55	0.01	8.54	0.02	8.54	0.03
3[a]	8.45	8.49	-0.04	8.33	0.12	8.40	0.05
10[a]	7.99	8.31	-0.32	8.38	-0.39	8.37	-0.38
15[a]	9.30	9.23	0.06	9.24	0.06	9.22	0.07
19[a]	8.85	9.17	-0.32	9.15	-0.30	9.14	-0.30
22[a]	8.48	8.82	-0.34	8.80	-0.32	8.74	-0.26

[a] Test set compounds

Table 10 Actual (Act) and predicted (Pred) pK_i values and the residuals (Δ) of the training set and test set molecules for the quadruple mutant type models.

Comp	Act pK_i	Model IV		Model V		Model VI		Model VII	
		Pred pK_i	Δ	Pred pK_i	Δ	Pred pK_i	Δ	Pred pK_i	Δ
1	6.37	6.73	-0.35	6.74	-0.36	6.51	-0.14	6.19	0.17
2	7.60	7.22	0.38	7.27	0.33	7.43	0.17	7.48	0.11
4	6.32	6.48	-0.16	6.38	-0.06	6.32	-0.00	6.38	-0.07
5	5.00	5.20	-0.21	5.19	-0.19	5.05	-0.05	4.93	0.06
6	7.40	7.21	0.18	7.19	0.21	7.22	0.18	7.22	0.17
7	7.16	6.95	0.20	6.97	0.19	6.98	0.18	7.15	0.01
9	5.61	5.74	-0.13	5.70	-0.09	5.60	0.01	5.74	-0.14
10	7.84	7.73	0.11	7.76	0.08	7.77	0.07	7.69	0.14
11	5.61	5.03	0.57	5.18	0.42	5.44	0.17	5.30	0.30
12	6.00	6.54	-0.54	6.38	-0.38	6.31	-0.31	6.21	-0.21
13	6.65	6.84	-0.19	6.98	-0.33	6.92	-0.27	6.76	-0.11
14	8.88	8.75	0.14	8.69	0.19	8.73	0.15	8.86	0.02
16	8.23	8.19	0.04	8.14	0.09	8.06	0.17	8.17	0.06
17	6.19	6.10	0.09	6.03	0.16	6.22	-0.03	6.15	0.03
19	6.91	6.90	0.01	6.89	0.02	6.84	0.07	6.99	-0.09
20	8.09	8.21	-0.11	8.23	-0.13	8.15	-0.06	8.13	-0.04
21	9.09	9.13	-0.04	9.21	-0.12	9.32	-0.23	9.19	-0.10
22	8.56	8.68	-0.12	8.72	-0.15	8.63	-0.06	8.26	0.05
24	8.34	8.30	0.04	8.24	0.10	8.42	-0.08	8.28	0.06
25	8.31	8.24	0.07	8.28	0.03	8.25	0.07	8.60	-0.04
3[a]	5.35	5.84	-0.49	5.86	-0.11	5.75	0.08	5.75	-0.40
8[a]	7.79	8.52	-0.73	8.56	-0.13	8.43	0.09	8.44	-0.65
15[a]	6.62	6.89	-0.28	6.74	0.08	6.82	0.07	6.95	-0.33
18[a]	8.11	7.52	0.59	7.68	-0.12	7.56	-0.04	7.43	0.68
23[a]	8.56	8.34	0.22	8.18	0.12	8.30	0.04	8.11	0.45

[a] Test set compounds

The representative CoMFA models of Cyc for the two types of *Pf*DHFRs were determined using the terms of r^2_{cv} and r^2_{nv}. By considering the statistical results of Cyc against the wild type in Table 2, only model III shows r^2_{cv} values higher than 0.66 and also gives the best r^2_{nv} (0.985). Consequently, CoMFA model III was used for further contour map discussion. In the case of the quadruple mutant enzyme, models IV-VI, with r^2_{cv} values higher than 0.66 (0.786, 0.729 and 0.676, respectively) were acceptable and the r^2_{nv} values were 0.983, 0.962 and 0.986, respectively. These results suggest that the three tested probes (C_{sp3}, O_{sp3} and H) produce qualitatively very similar models. The results also suggest that all three types of probes are equally important in the enzyme-ligand interactions. The combination of the three probe atoms was then used, resulting in model VII with r^2_{cv} = 0.786 and r^2_{nv} = 0.979. Thus, based on the CoMFA of the Cyc derivatives against the wild type *Pf*DHFR, the best model is Model III using a probe atom H(+1) with r^2_{cv} = 0.727, S_{press} = 0.322, noc = 6, r^2_{nv} = 0.985, s = 0.075, and F value = 144.780. The combination of the three probe atoms in model VII gave satisfactory results in terms of r^2_{cv} = 0.786, S_{press} = 0.650, noc = 5, r^2_{nv} = 0.979, s = 0.202, F value = 132.386, and so was the best model slective by the CoMFA of the Cyc derivatives with the mutant enzyme.

The graphical plots between the actual and the predicted pK_i of the training set and the test set of both the wild type and quadruple mutant type CoMFA models are ploted in Figure 26 (A) and (B), respectively. In the CoMFA, model III had steric and electrostatic contributions of 56.5% and 43.5%, respectively. For the CoMFA with model VII, the steric contribution increased to 67.8 %. This implies that the steric property is more effective against the activities of the Cyc compounds in the mutant enzyme compared with the wild type enzyme.

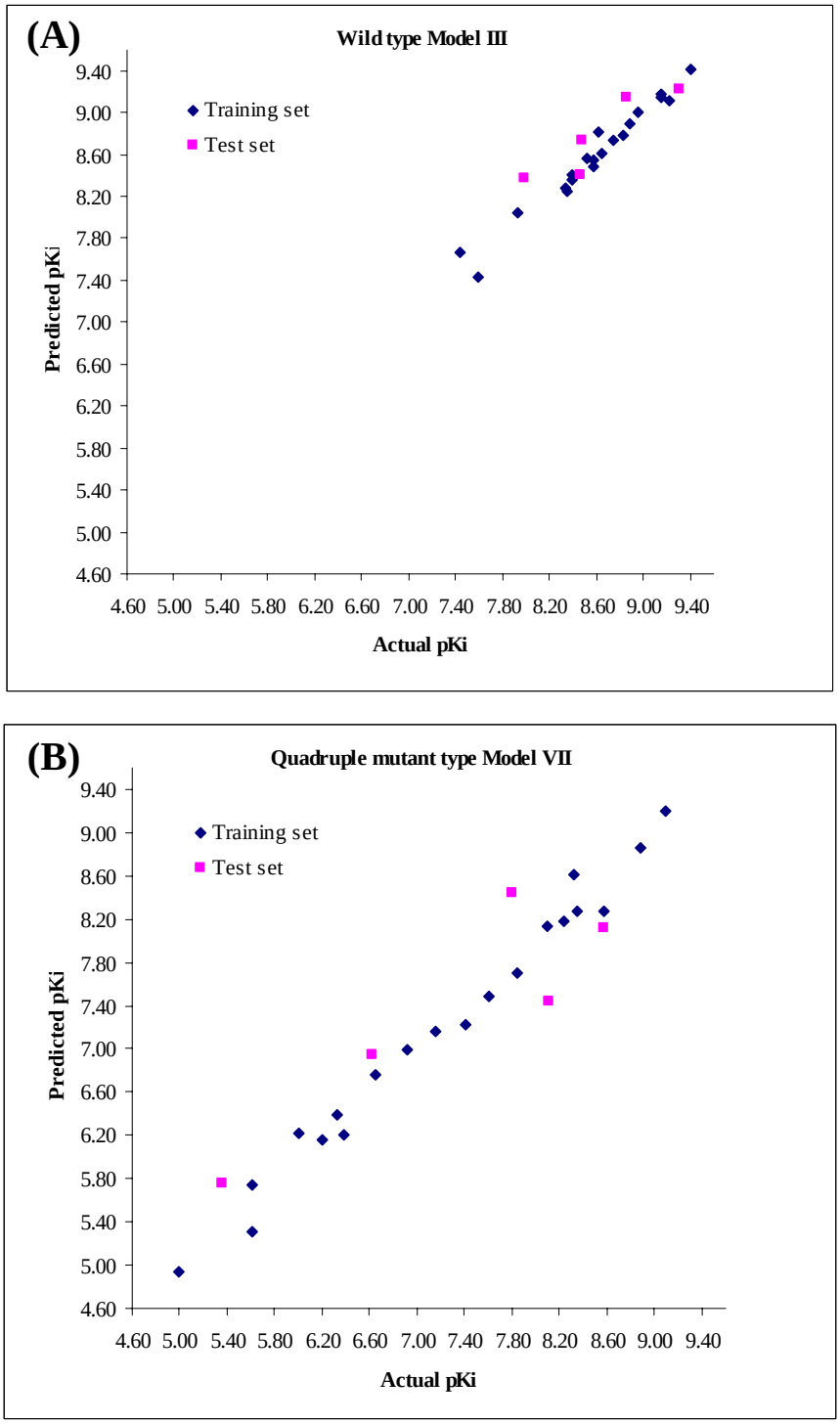

Figure 26 Ploted graph of the predicted vs actual activities of the training set and the test set molecules (A) wild type-Model III (B) mutant-Model VII

2.2 CoMFA contour maps

The resultant CoMFA contours were merged into the binding pocket of the two enzyme targets; namely the the wild type and quadruple mutant type *Pf*DHFRs. The template compound **14** was selected to display in the merged CoMFA contour maps.

The CoMFA steric and electrostatic fields based on PLS analysis are represented as three-dimensional contour plots for the wild type (Figure 27 and Figure 28) and the quadruple mutant type (Figure 29 and Figure 30). The steric contour map indicates areas in which the molecular steric bulk might have a favourable (green) or unfavourable (yellow) effect on the activity of an analogue. The electrostatic contour map displays blue contours to refer positive charge-favouring areas and red contours to indicate negative charge-favouring areas.

For the CoMFA contour plots of the wild type *Pf*DHFR, the steric contour (Figure 27) shows two green regions closed to the **Y** and $\mathbf{R_2}$ substitutions which indicate that the bulky groups are preferred in these positions to give higher activity. There is a yellow region near the $\mathbf{R_1}$ substitution, which implies the bulky substituents are likely to decrease the activity effect. Figure 28 shows the red regions near the 2- and 4- amino groups of the triazine ring and along the side chain of the $\mathbf{R_2}$ substitution. The blue areas are close to the **X**, **Y**, substitutions and the 2-amino of triazine ring positions. All steric-electrostatic contour plots are favorably consistent with the experimental data. The Cl substitute at the **Y** position gives a higher activity than the H atom, the long side chain with the O atom in the middle shows good activity, the 2- and 4- amino groups of the triazine ring can interact as a H-bonding interaction with Asp54, Ile14 and Ile164, and the more bulky groups, rather than with CH_3 which is not favorable at the $\mathbf{R_1}$ substitution.

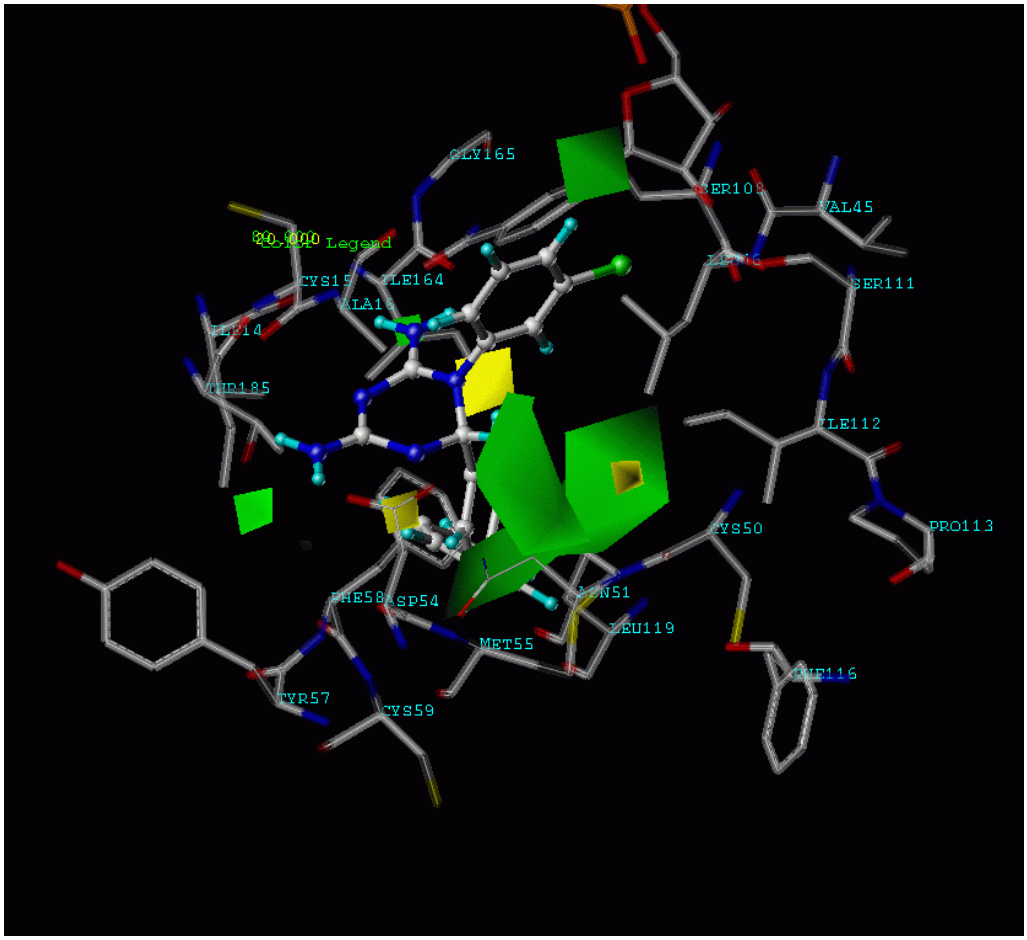

Figure 27 The steric contour maps of wild type *Pf*DHFR CoMFA model (st.dev. × coeff.). The favorable steric areas (contribution levels 80%) with more bulk are indicated by green regions, where as the disfavorable steric areas (contribution levels 20%) are shown by yellow regions. The compound **14** is represented by ball and stick.

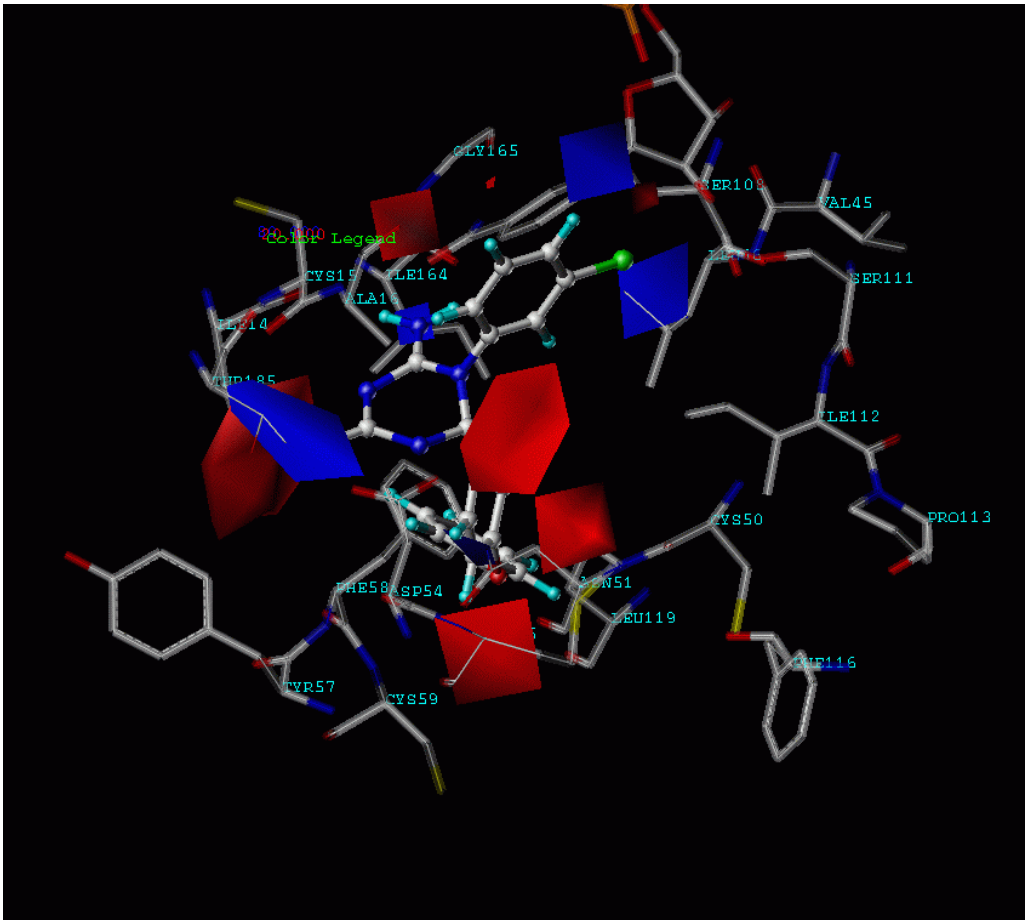

Figure 28 The electrostatic contour maps of wild type *Pf*DHFR CoMFA model (st.dev. × coeff.). The favorable electrostatic areas (contribution levels 80%) with positive charges are indicated by blue regions, whereas the favorable electrostatic areas (contribution levels 20%) with negative charges are show by red regions. The compound **14** is represented by ball and stick.

In the case of the CoMFA quadruple mutant steric contour map (Figure 29), the major sterically-favoured green regions are found near the **X** or *meta*-phenyl ring and the $\mathbf{R_2}$ substitution. On the other hand, there are yellow unfavoured steric regions close to the $\mathbf{R_1}$ substitution and the **Y** or *para*-phenyl ring. For the electrostatic contours (Figure 30), the **X** position favoured negative charge substitutes displayed as the red color. Regarding the positive charge electrostatic represented by the blue contour, there are regions around $\mathbf{R_2}$ and the 2-amino group of triazine ring suggesting that the substitutes with low electron density would give a higher level of activity. The distributions of the steric and electrostatic contours are supported by experimental data; with the Cl substitute at the **Y** position showing lower activity than the H atom which accorded to favorably non-sterical and positive charge at this region. Inaddition, there are sterical and negative charge favours at **X** in the phenyl ring substituting with Cl gives higher activity than for H. The $\mathbf{R_2}$ position favours bulkly groups with low electron densities whereas these groups are not favored in the wild type model. Consequently, compound **21** shows a higher level of activity than the compounds that have bulkly groups with high electron densities substitutes, and $\mathbf{R_1}$ shows unfavourable steric distribution, the same as in the wild type CoMFA steric contour.

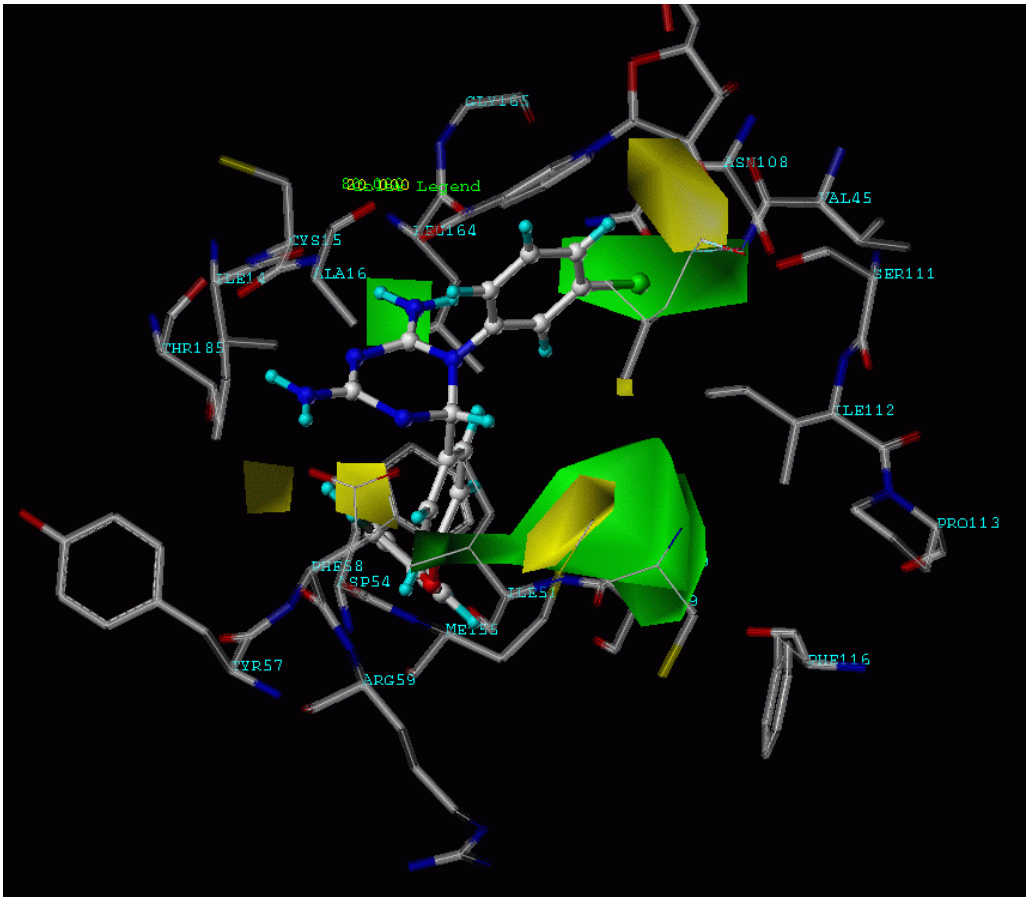

Figure 29 The steric contour maps of quadruple mutant type *Pf*DHFR CoMFA model (st.dev. × coeff.). The favorable steric areas (contribution levels 80%) with more bulk are indicated by green regions; where as the disfavorable steric areas (contribution levels 20%) are shown by yellow regions. The compound **14** is represented by ball and stick.

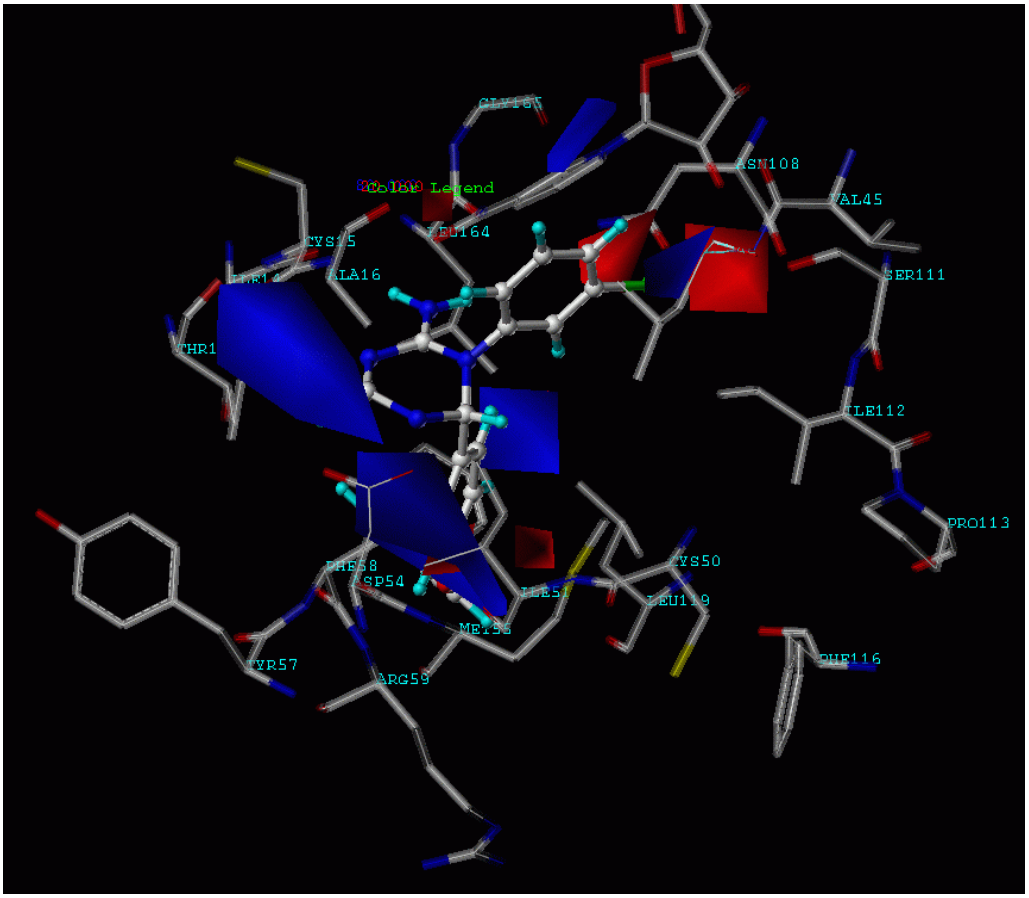

Figure 30 The electrostatic contour maps of quadruple mutant type *Pf*DHFR CoMFA model (st.dev. × coeff.). The favorable electrostatic areas (contribution levels 80%) with positive charges are indicated by blue regions, whereas the favorable electrostatic areas (contribution levels 20%) with negative charges are show by red regions. The compound **14** is represented by ball and stick.

2.3 Comparison of Particular Interaction Energies of the Cyc Compound With the Wild Type and the Mutant Enzymes

The interactions between individual amino acids and Cyc of the wild type and the quadruple mutant *Pf*DHFR binding pockets were investigated using MP2/6-31G(d,p) level of calculations, followed by the BSSE-CP energy corrections. The obtained corrected interaction energies of Cyc which surrounding the binding pocket of both the wild type and the quadruple mutant enzymes are plotted in Figure 31 (A) and (B), respectively.

Asp54 shows the strongest interaction energy with the wild type and the mutant enzymes. In molecular level investigation, the Asp54 is formed a strong H-bonded interaction with the 2-amino group. Ile14 also formed H-bonded interaction with the 4-amino group. In the case of Phe58, it could be presented as a *pi-pi* interaction between the phenyl ring of Phe58 and the 1,3,5-dihydrotriazine ring of the inhibitor. Figure 32 shows the main attractive amino acids, Asp54, Ile14, Ile14Leu, and Phe58, and the Cyc which are in the binding sites of the wild type and the quadruple mutant type.

The two mutations at Asn51Ile and Cys59Arg did not have any significantly different interaction with Cyc in both the wild type and the mutant enzyme. Although Ile164 mutated to Leu164, its back bone amino acid still produced H-bonded interaction with the 4-amino group of the 1,3,5-dihydrotriazine ring. Finally, changing Ser to Asn at the 108 position showed the largest difference in repulsive interaction energy of approximately 4 kcal/mol. This is due to a steric clash between the *p*-Cl phenyl substitute of Cyc and the larger side chain of Asn108 as shown by the Van der Waal surface in Figure 33. This evidence is corresponding to the different favourable wild type and mutant type CoMFA contour map of **Y** position.

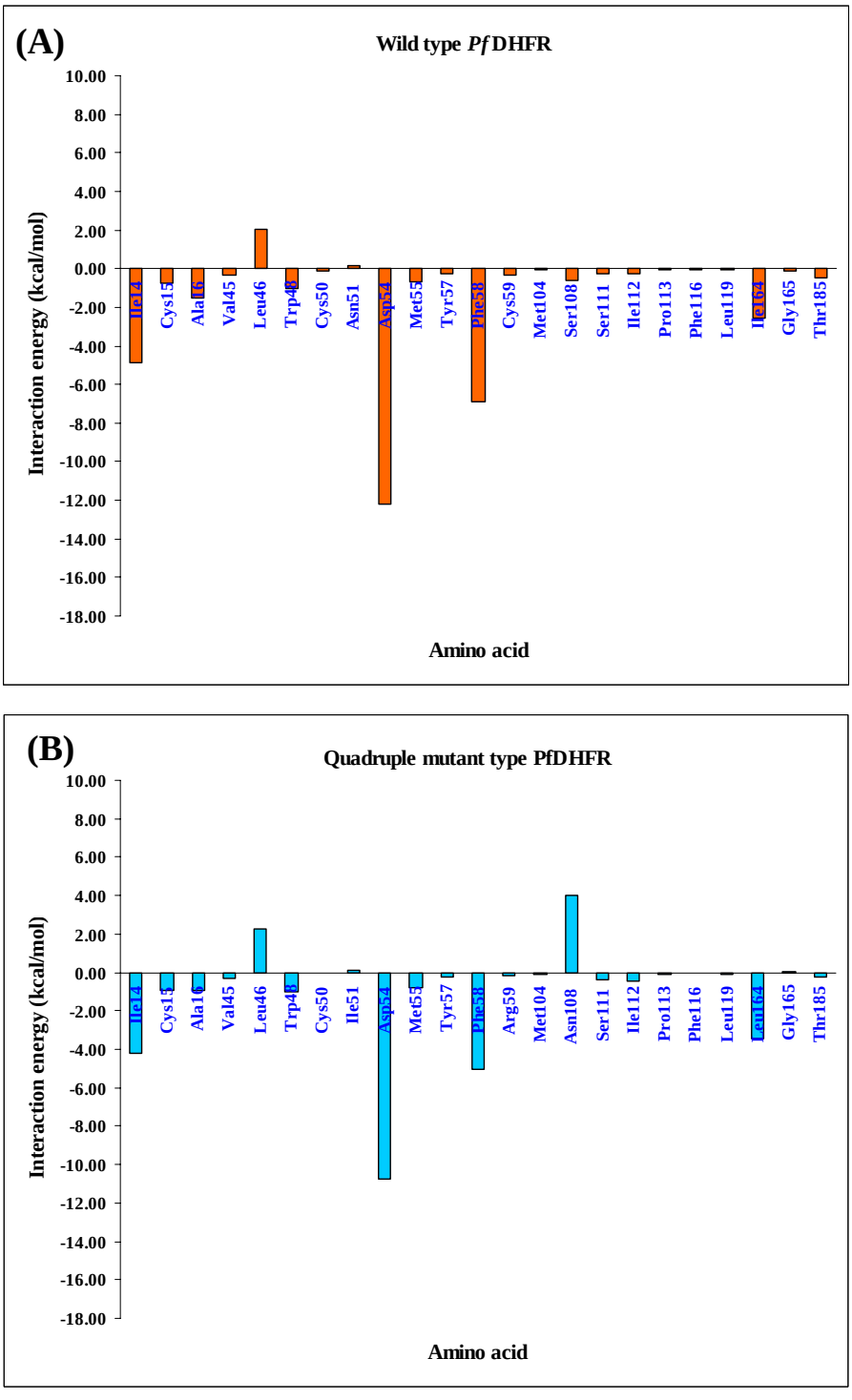

Figure 31 The obtained MP2/6-31G(d,p) with BSSE-CP interaction energies of Cyc and individual amino acids surrounding the binding pocket of wild type (A) and quadruple mutant type (B) *Pf*DHFRs

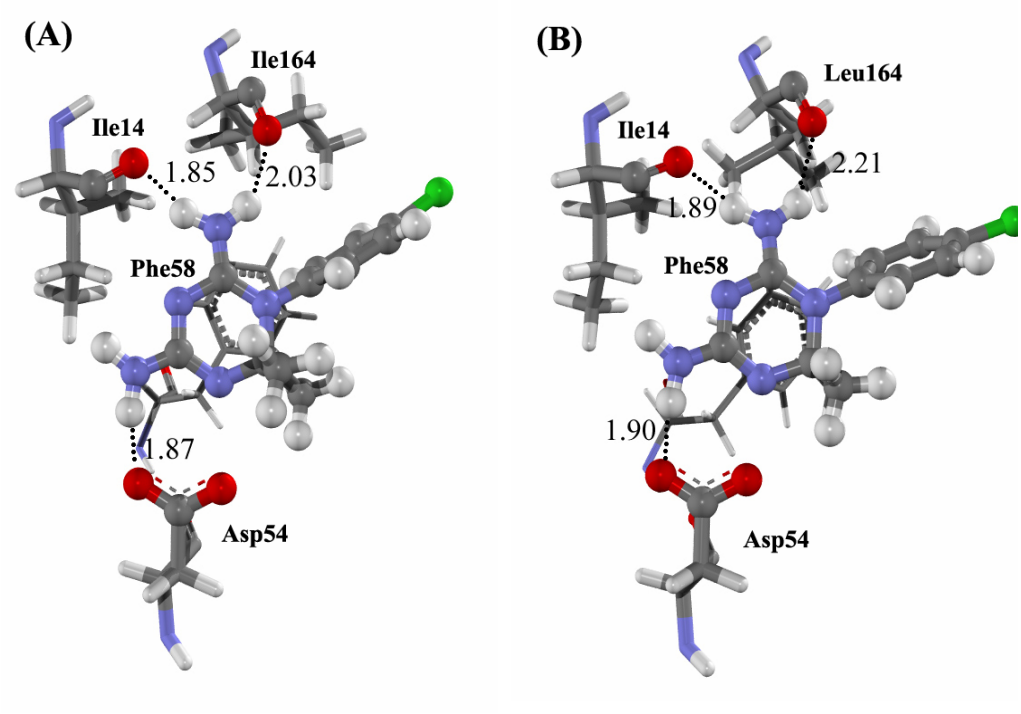

Figure 32 H-bond distances between Cyc inhibitor and residues in the binding pocket; (A) wild type and (B) quadruple mutant type DHFRs (in Å).

(A) **(B)**

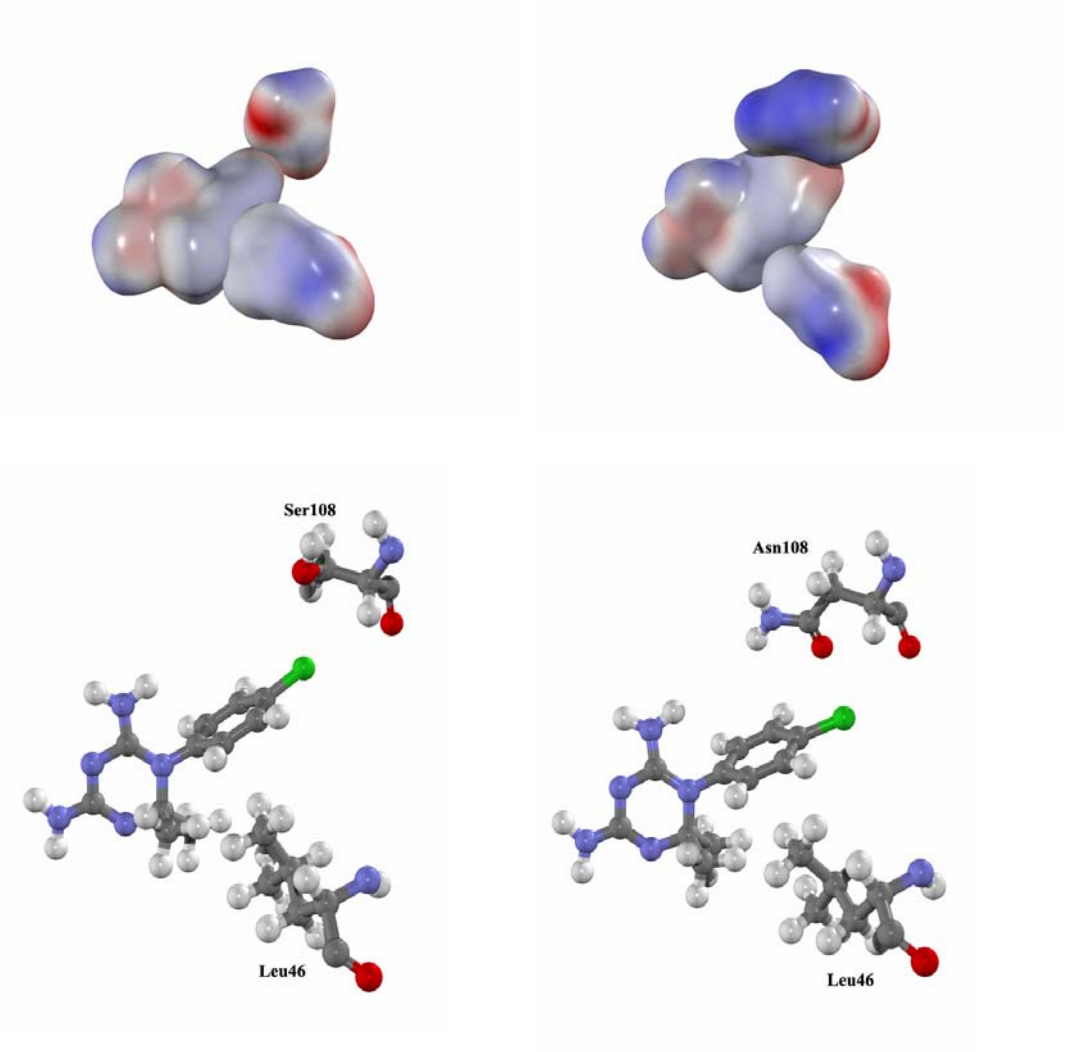

Figure 33 The electrostatic potential is shown on the van der Waal surface as red for negative and blue for positive values for Cyc and Ser108 (A) and Asn108 (B).

2.4 Different Interaction Energies between the Cyc and the WR99210 Inhibitors

WR99210 is a good inhibitor against both wild type and quadruple mutant type *Pf*DHFRs because of the greater flexibility of side chains. The individual interaction energy of the WR99210 inhibitor bound into the two target enzymes of *Pf*DHFRs was calculated by following the Cyc steps of calculations detailed above in the AMBER molecular mechanical minimization and Quantum chemical calculations sections of this paper.

The energy comparisons between the Cyc and the WR99210 inhibitors in both the wild type and the quadruple mutant type *Pf*DHFR are depicted in Figure 34 (A) and (B), respectively. Most of the amino acids of the wild type and the mutant *Pf*DHFRs surrounding the inhibitors show the same trend of interaction energy, except for the two amino acids, Leu46 and Asn108, which give repulsive interaction energy for the Cyc inhibitor in the mutant model. However, the flexible WR99210 inhibitor has higher attractive energy in summation than the rigid Cyc inhibitor. Of particular note is the fact that the basic structural information proves that the cause of the Cyc resistances in the quadruple mutant type *Pf*DHFR came from the steric clash of the Asn108 mutation with the repulsive interaction energies as shown in Figure 34 (B), similar to that found with pyr. On the other hand, the potent WR99210 inhibitor can avoid the steric clash with Asn108, so, it does not generate any positive energy value. In conclusion, quantum chemical calculations can be applied to investigate the relative levels of specific interaction energy of different DHFR inhibitors at a molecular level in the biomolecular systems.

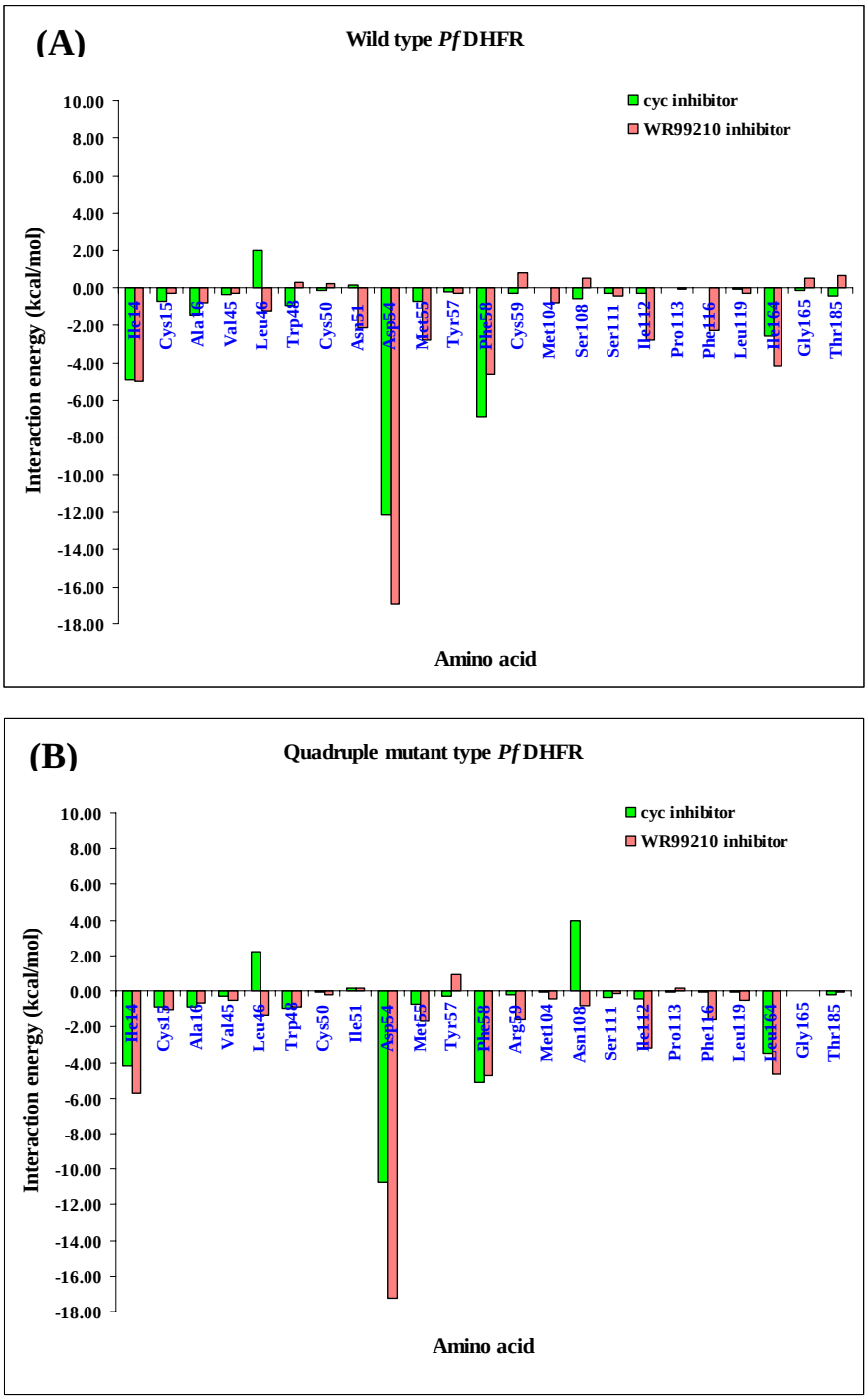

Figure 34 The MP2/6-31G(d,p) with BSSE-CP energetic comparison between Cyc and WR99210 in case of (A) wild type and (B) quadruple mutant type *Pf*DHFR binding sites

3. Different Binding Energies of Cycloguanil, Pyrimethamine and WR99210 Antifolates to Quadruple Mutant Type *Pf*DHFR, Based On Three-Layer ONIOM Method

3.1 Molecular Dynamics Structural Comparison of Three Antifolates Complex with Quadruple Mutant *Pf*DHFR

The geometries of Pyr, Cyc and WR99210 antifolates complexed with quadruple mutant were simualted using AMBER molecular dynamics simulations with duration time 500 ps. The obtained ligand/enzyme simulating sytems shall be evaluated for further ONIOM energy calculations. Evaluation of structural molecular dynamics drift is provided for analyzing root mean square deviations (RMSDs) of both protein and ligand as a function of simulation time. Hence, the RMSDs of Pyr, Cyc and WR99210 antifolates are plotted in Figure 35.

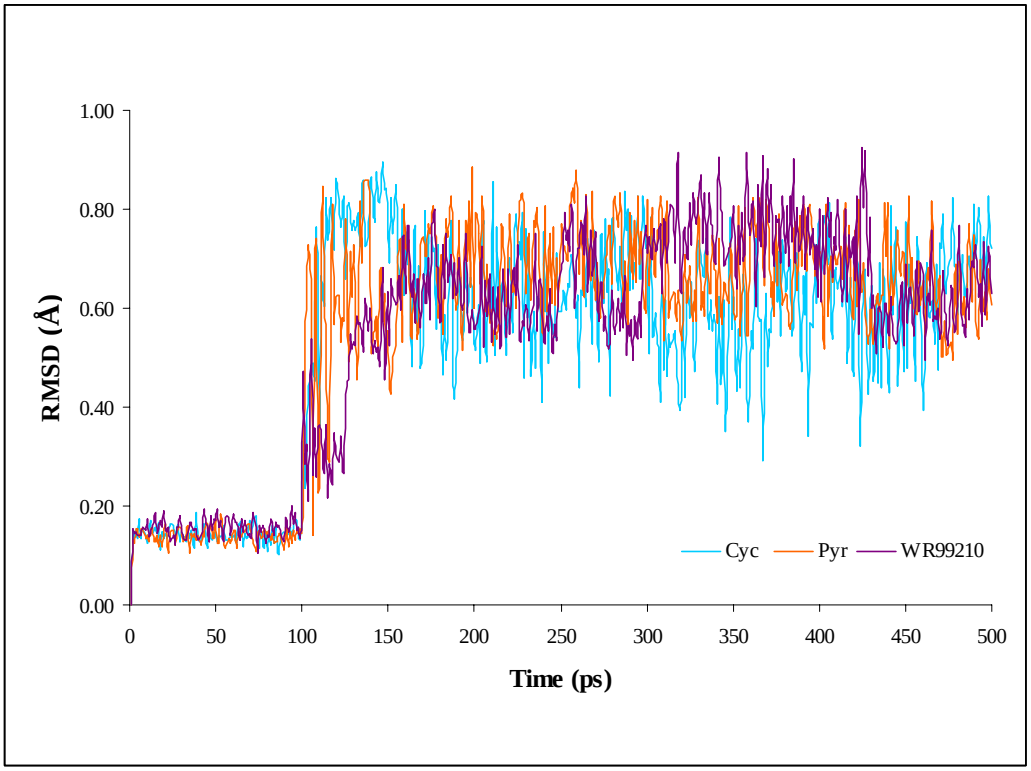

Figure 35 RMSD of the three antifolates: Cyc (blue line), Pyr (orange line) and WR99210 (purple line) in Å

Then, their quadruple mutant type *Pf*DHFR proteins of three antifolates based on the backbone amino acids selections are plotted with 500 ps simulation times as shown in Figure 36. They seem that the results show the same pattern with that of RMSDs of all antifolates less than 1 Å and their proteins less than 2.0 Å. After md1 (0-100 ps), RMSDs of all three antifolates quickly reach an equilibration after about 150 ps simulation time which can be implied that our complex structures obtained at 500 ps can be used for further binding energy calculations

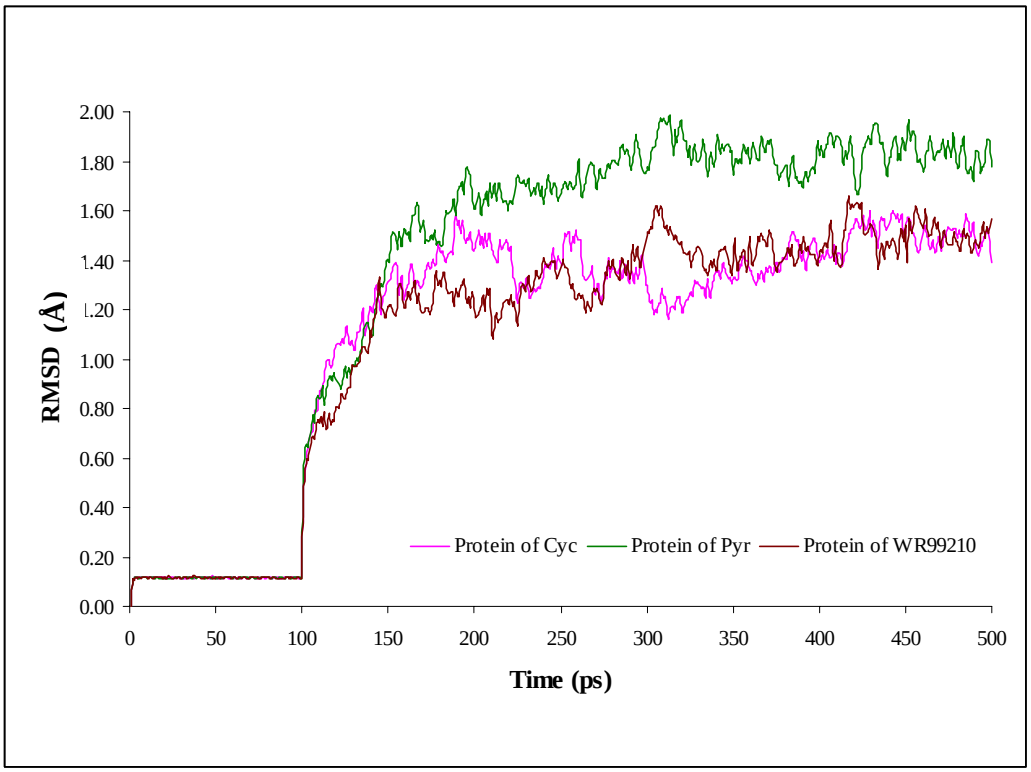

Figure 36 RMSD of the back bond amino acids atoms from the quadruple mutant *Pf*DHFR obtained from the complex structures: Cyc (pink line), Pyr (green line) and WR99210 (brown line)

3.2 ONIOM Extrapolated Binding Energy of Three Antifolates Complex with Quadruple Mutant *Pf*DHFR

The extrapolated binding energies of three antifolates bound in the quadruple mutant type *Pf*DHFR using the ONIOM3 method are given in Table 11. Based on the meaning of binding energy (ΔE) calculating from different energy of the inhibitor-enzyme complex and the combination energies of ligand and enzyme, the explanable energy can be written by ONIOM3 energy components as follow:

$$\Delta E_{real}^{ONIOM3} = \Delta E_{real}^{MM} + \Delta E_{intermediate}^{LQ} + \Delta E_{small}^{HQ} - \Delta E_{int\,ermediate}^{MM} - \Delta E_{small}^{LQ} \quad (10)$$

$$\Delta E_{real}^{ONIOM3} = \left[\Delta E_{real}^{MM} - \Delta E_{int\,ermediate}^{MM}\right] + \left[\Delta E_{intermediate}^{LQ} - \Delta E_{small}^{LQ}\right] + \Delta E_{small}^{HQ} \quad (11)$$

$$\Delta E_{real}^{ONIOM3} = \Delta E_{small}^{HQ} + \Delta\Delta E_{intermediate\text{-}small}^{LQ} + \Delta\Delta E_{real\text{-}intermediate}^{MM} \quad (12)$$

where ΔE_{small}^{HQ} denotes the interaction energy of small region using B3LYP/6-31G(d,p) level of calculations. The $\Delta\Delta E_{intermediate\text{-}small}^{LQ}$ is the interaction energy between intermediate and small regions, calculated at the PM3 semiempirical method. The last term of $\Delta\Delta E_{real\text{-}intermediate}^{MM}$ is the molecular mechanics UFF interaction between real and intermediate layers.

Table 11 ONIOM3 Energy terms in kcal/mol for antifolate ligands bound in the same binding pocket in quadruple mutant type *Pf*DHFR.

Ligands	ΔE_{real}^{ONIOM3}	ΔE_{small}^{HQ}	$\Delta\Delta E_{intermediate\text{-}small}^{LQ}$	$\Delta\Delta E_{real\text{-}intermediate}^{MM}$
Pyr	-64.87	-33.38 (51%)	-18.40 (28%)	-13.08 (20%)
Cyc	-69.84	-36.57 (52%)	-19.61 (28%)	-13.66 (19%)
WR99210	-96.23	-53.77 (56%)	-29.42 (31%)	-13.04 (13%)

The value in parenthesis is the percentage of energy contributed to the total energy.

The ΔE_{real}^{ONIOM3} of WR99210 shows strongest total extrapolated binding energy. The total binding energies of Pyr and Cyc are resulted less than the WR99210 with significantly different values by approximately 31 and 26 kcal/mol, respectively. Although the total binding energy of potent WR99210 shows the best interaction for the quadruple mutant type *Pf*DHFR but the other explanable ONIOM3 energies are also important for further more details.

Considering the ΔE_{small}^{HQ} of potent inhbitor WR99210 for quadruple mutant *Pf*DHFR, it shows the highest energy contribution (56%) of total ONIOM3 energy comparing with Pyr and Cyc inhibitors by appproximately 5% and 4%, respectively. Deeply in molecular details of small layer, Leu164 produces the hydrogen bonded interaction with 4-amino group of all inhbitors. In addition, Asp54 forms both electrostatic and hydrogen bonded interactions with N1 and 2-amino group of Pyr, Cyc and WR99210 antifolates as displayed Hydrogen bonded distances in Figure 37 (A), (B) and (C), respectively.

On the other hand, Asn108 showed the repulsive interaction energy for Pyr and Cyc by approximately 4 kcal/mol (see in Table 3) which caused from the steric clash between the *p*-Cl phenyl substitute of Pyr or Cyc and the side chain of Asn108. However, these evidences are not found in the case of the flexible WR99210 inhibitor, because it avoids the steric clash with Asn108 which effected to higher ΔE_{small}^{HQ} energy compared with Pyr and Cyc inhibitors. The steric clash effects are shown by the van der Waal surface of three antifolate inhibitors and Asn108 in Figure 38.

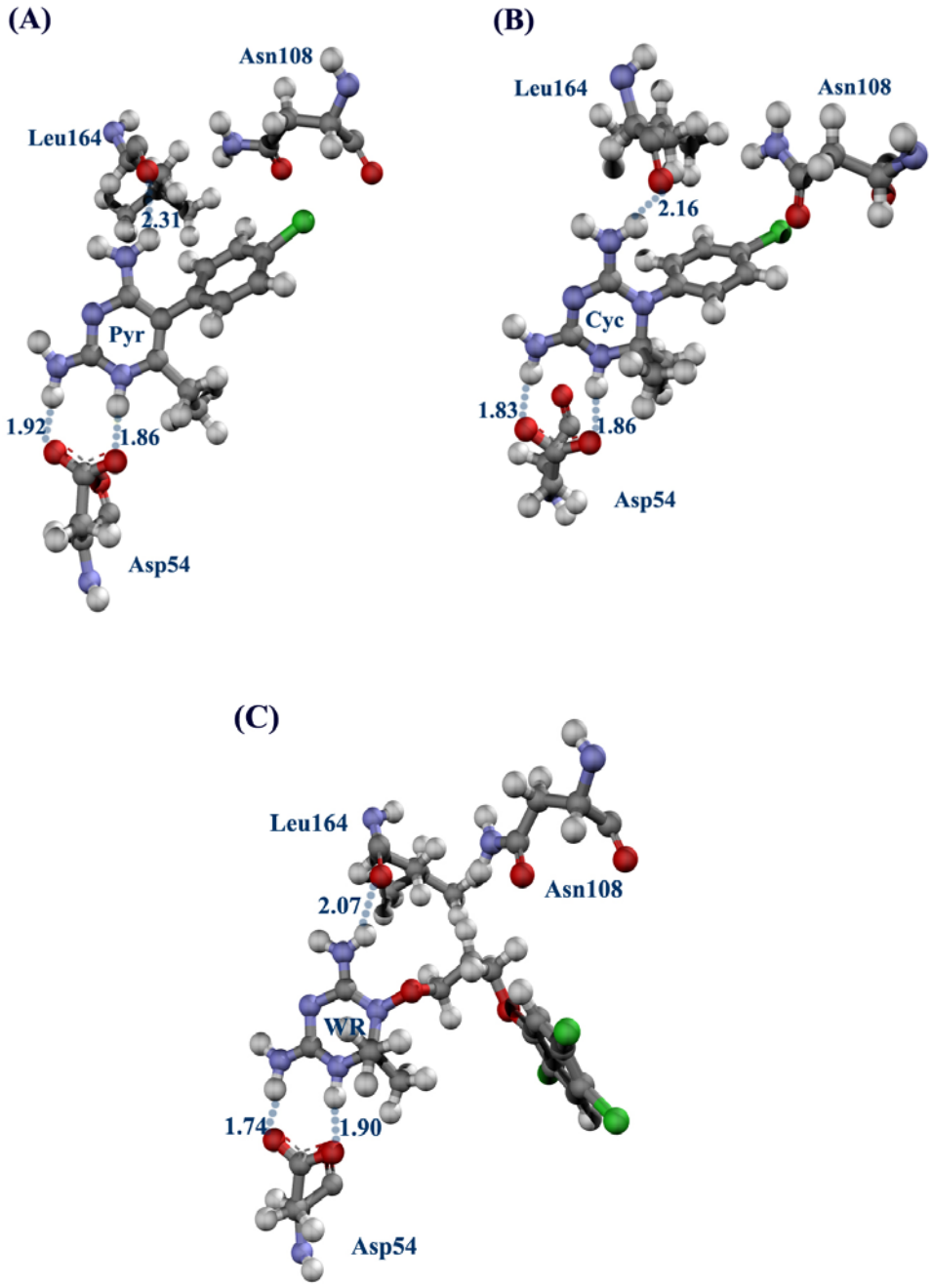

Figure 37 H-bond distances between small regions of quadruple mutant *Pf*DHFR binding pocket and ligands (A) Cyc (B) Pyr and (C) WR99210 (in Å).

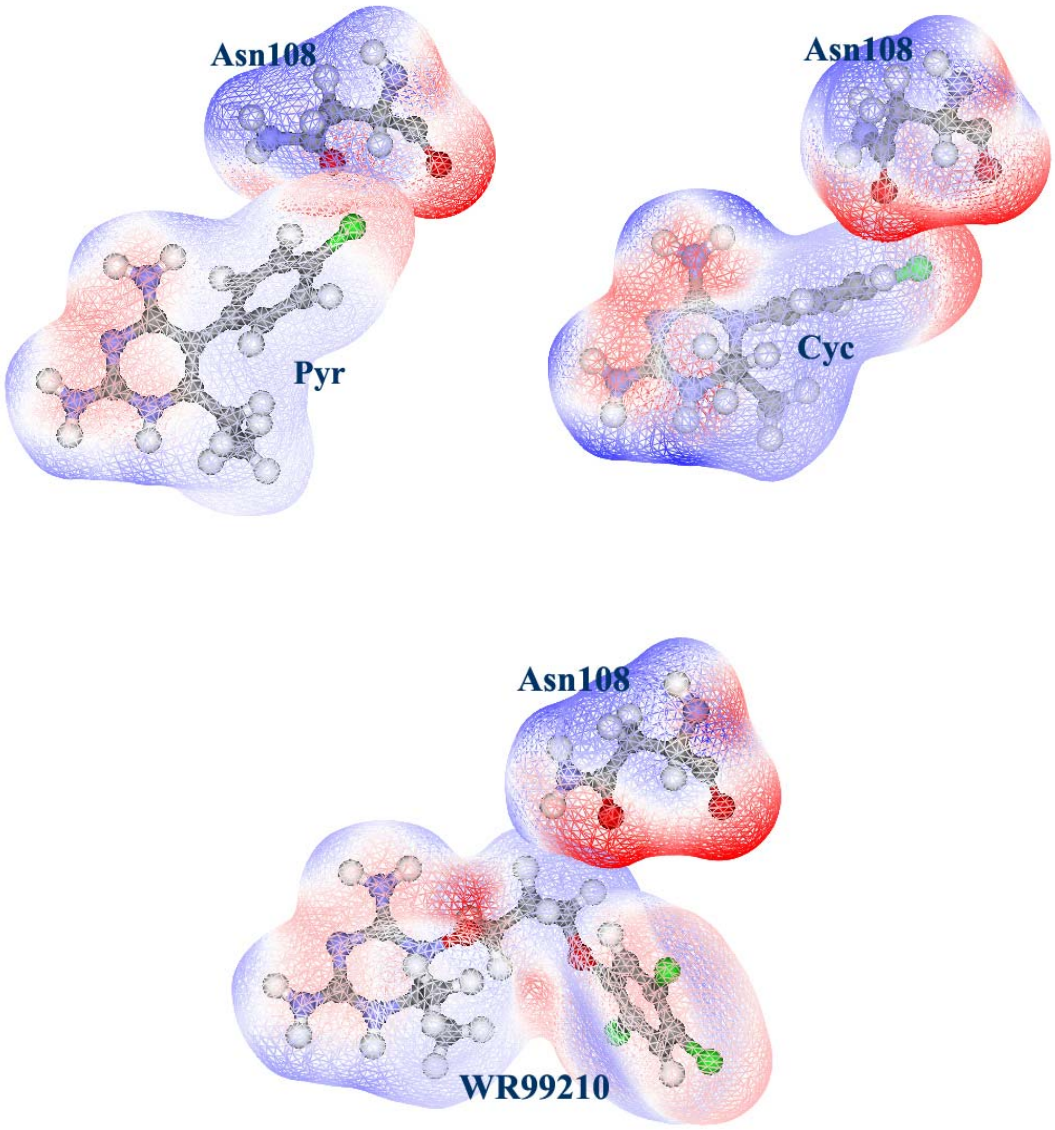

Figure 38 Electrostatic potential is shown on the van der Waal surface as red for negative and blue for positive values for Asn108 and three types of antifolates, Pyr, Cyc and WR99210.

For the $\Delta\Delta E^{LQ}_{intermediate\text{-}small}$ energy term of Pyr and Cyc are equally contributory energy with estimated 28% of total interactions. The WR99210 gives the strongest $\Delta\Delta E^{LQ}_{intermediate\text{-}small}$ energy for the intermediate region of amino acids surrounding the binding pocket within 4 Å interatomic distances interacted with WR99210, except three amino acids of the small region. Based on the large molecule of WR99210, it can be more interacted with amino acids in the intermediate layer which led to higher percentage of $\Delta\Delta E^{LQ}_{intermediate\text{-}small}$ to the total ONIOM3 energy comparing with smaller Pyr and Cyc inhibitors.

The $\Delta\Delta E^{MM}_{real\text{-}intermediate}$ terms of all three antifolate inhibitors are equivalent energies by approximately 13 kcal/mol. Although they have the equal interaction energy for remaining residues excluding twenty-three residues in small and intermediate layers, but they also have the different percentage energy contributions. The molecular mechanic UFF energy of real system for WR99210 ligand shows less influential energy to the total binding energy.